PRELIMINARY EXPERIMENTAL STUDIES ON SYNTHESIZING TiFe INTERMETALLIC COMPOUNDS BY POWDER METALLURGY ROUTE

Irina STURZEANU[1]*, Mariea DEACONU [2], Marioara ABRUDEANU[3], Valentin OLARU[4], Daniel PAPARAGICĂ[5], Iulia DUMITRESCU[6], Aurel DAVID[7]

The integration of renewable energy requires efficient storage solutions, including hydrogen storage, a key and timely element for the energy transition. This paper presents results on the synthesis of TiFe intermetallic compound using powder metallurgy route. The experimental approach, process parameters, and the analysis techniques to identify the compound and assess limitations were presented. The analyses of the obtained samples confirmed the partial formation of the TiFe phase, demonstrating the process feasibility. Optimizing the technological parameters can yield to efficient formation of the TiFe intermetallic phase in a higher proportion, thus obtaining an advance material for hydrogen storage in new energy technologies.

Keywords: TiFe, intermetallic compound, powder metallurgy, hydrogen storage.

1. Introduction

Concern over hydrogen's potential role in energy systems is globally growing. Several studies have suggested that hydrogen could be used in nearly every aspect of the energy system, evaluations demonstrating that it is a practical and affordable option for decarbonization [1]. One of the main topics in the energy sector is the development of safe and efficient materials for storing hydrogen isotopes. The use of hydrogen (protium isotope) and, implicitly, its storage has attracted more attention recently due to the need to limit and reduce global warming, as well as the need to find fuel and energy sources that no longer contribute to environmental pollution and do not use finite natural resources. For tritium isotope,

[1]* Ph.D. Student, National University of Science and Technology POLITEHNICA Bucharest – Doctoral School of Materials Science and Engineering, Romania, Corresponding author: irina.paraschiv@nuclear.ro
[2] Scientific Researcher, RATEN Institute for Nuclear Research Pitesti, Romania
[3] Prof., National University of Science and Technology POLITEHNICA Bucharest, Romania
[4] Scientific Researcher, RATEN Institute for Nuclear Research Pitesti, Romania
[5] Eng., RATEN Institute for Nuclear Research Pitesti, Romania
[6] Scientific Researcher, RATEN Institute for Nuclear Research Pitesti, Romania
[7] Scientific Researcher, RATEN Institute for Nuclear Research Pitesti, Romania

which is radioactive, the interest is in nuclear field (in nuclear fission and fusion reactors).

Fig. 1 presents the known methods by which hydrogen can be stored. Pressure tanks that are pressured to several hundred atmospheres are used for hydrogen gas storage. The only way to store hydrogen in liquid form is at cryogenic temperatures, which requires a lot of energy. The poor volumetric storage density of hydrogen is a drawback of both approaches. An efficient and attractive method for storing hydrogen is solid storage in materials. This method uses materials that can absorb or adsorb hydrogen.

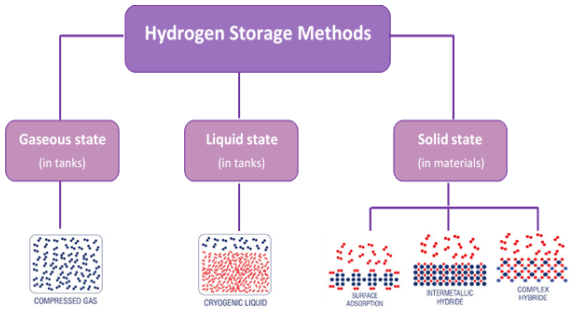

Fig 1. Hydrogen storage methods Adapted from ref. [2]

Metal hydrides are the most explored and promising materials for solid-state hydrogen storage. In these materials, the metal absorbs hydrogen by the process of absorption, forming a hydride that releases hydrogen when heated [3]. Equation (1) describes the typically reversible process that forms metal hydrides:

$$M + \frac{x}{2} H_2 \leftrightarrow MH_x + \Delta H \quad (1)$$

where: M is the metal, MH_x is the metal's hydride, x represents the stoichiometric ratio of hydrogen to metal, indicating how many hydrogen atoms are bonded to each metal atom and ΔH is the formation enthalpy [4].

Fig. 2 illustrates how the interaction between the metal and hydrogen takes place, leading to the metal hydride formation. As it can be observed, hydrogen absorption in the metal is a process that takes place in multiple steps [4]:

- exposure of the metal to hydrogen and the closeness of H_2 molecules to its surface;
- attraction of H_2 molecules to the metal surface via van der Waals forces and physisorption of hydrogen molecules on the metal surface;
- dissociation of the physiosorbed molecular hydrogen into atomic hydrogen through prolonged gas exposure and temperature conditions;
- the subsurface layer's interstitial positions are occupied by hydrogen atoms that enter the host metal lattice by chemisorption;

- hydrogen diffuses into the metal lattice, forming a solid solution M-H, named α phase (H/M < 0,1);
- the hydride phase MH_x, also known as the β phase, is formed [5], [6], [4], [7].

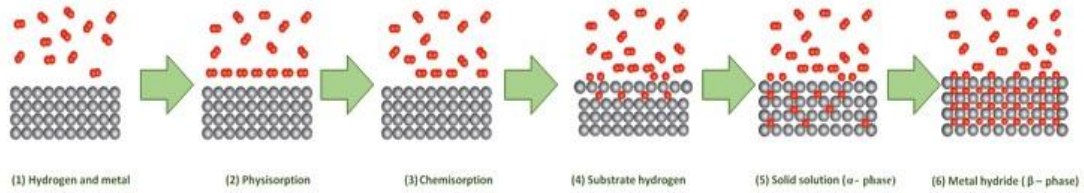

Fig 2. Metal hydride formation steps
Adapted with permission from ref. [4] Copyright 2019, Springer Nature Switzerland

A metal (cation) and hydrogen (containing the anion) form the structure of metal hydrides. As was previously said, chemical bonding occurs after hydrogen chemisorption, this making possible the storage of hydrogen as hydrides. Fig. 3 illustrate a classification of metal hydrides for hydrogen storage.

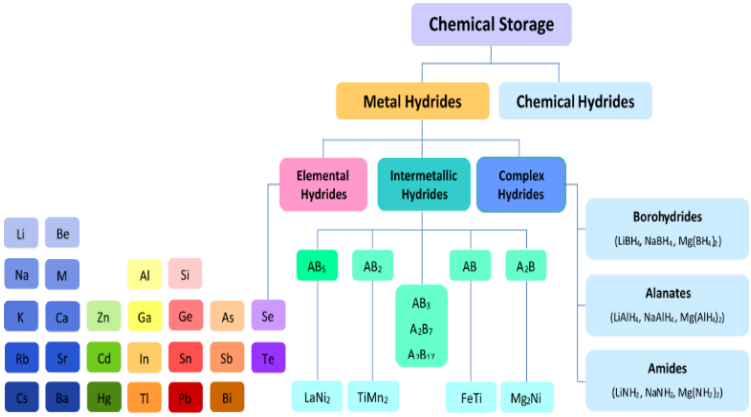

Fig 3. Types of metal hydrides used for solid state hydrogen storage

Adapted: from ref. [8]; from ref. [9] © 2019, with permission from Elsevier; from ref. [10] © 2021, with permission from American Chemical Society; from ref. [11] ©2024, with permission from Wiley-VCH GmbH.

Intermetallic hydrides are metal or alloy hydrides (also known as hydrogen storage/absorption alloys), formed by transition metals, in which hydrogen occupy tetrahedral and/or octahedral interstitial positions via metallic bonds. Pure metals tend to form stable elemental hydrides, which releases hydrogen above 400°C. In contrast, alloys containing a transition metal that do not form hydrides at low temperatures exhibit reduced thermodynamic stability [12].

Among many intermetallic compounds described in the literature for reversible stationary hydrogen storage applications in ambient conditions, TiFe (known as an AB type intermetallic compound [12] have recently gained growing interest. The high hydrogen storage capacity (gravimetric capacity of ~1.9 wt. % and volumetric capacity of 105 kgH2 /m3), good sorption and desorption kinetics, reaction reversibility, and capacity to operate in conditions near room temperature and atmospheric pressure make the intermetallic compound TiFe suitable for use in real-world applications. Additionally, TiFe alloys' availability of raw materials leads to low production and material costs, compared to other intermetallics [13], [14], [15], [16].

The hydrogen storage properties of TiFe intermetallic compound are strongly linked with the composition of the alloy and the presence of secondary phases [13]. It is known that Ti and Fe have close melting points (Ti - 1670 °C [17], Fe – 1538 °C [18]). Regarding the alloy, as it can be observed from TiFe phase diagram (Fig. 4), TiFe intermetallic compound presents a narrow compositional range, with the largest domain from 49.7 to 52.5 at% Ti, at 1085 °C eutectic temperature [13]. The crystal structure of TiFe was identified by Laves et al. as CsCl-type (B2, space group $Pm\bar{3}m$) [19].

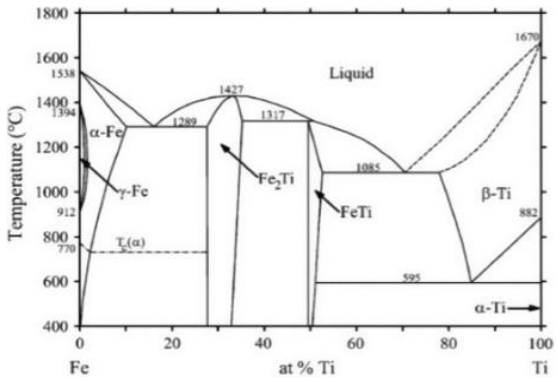

Fig 4. TiFe phase diagram

Reproduced from ref. [13] CC-BY - NC License

Given the attractive properties of TiFe alloys, reducing the production and manufacturing cost is a continuing and primary research subject.

Among the synthesis methods for Ti alloys (arc or induction melting, mechanical alloying, cold rolling, etc.) powder metallurgy is a potentially cost-effective alternative. It is a near-net-shape manufacturing technology, and includes the production of powders, compaction and shaping of powders, sintering, and also post sintering processes to fabricate the final product [20]. Several research studies

mention the possibility of obtaining Ti alloys with various Fe contents through powder metallurgy, some of which can be found in references [21 - 26].

Having this entire context in mind, it can be said that, in order to overcome the challenges posed by hydrogen storage in solid-state materials, storage materials must be developed and optimized. Because the area is so broad, it is required research and evaluate a wide range of materials, their obtaining methods, and also, to develop strategies for enhancing the hydrogen properties of the materials [27].

In light of this, the purpose of the present scientific paper is to obtain TiFe intermetallic compound by powder metallurgy method, material known for its hydrogen storage applications.

2. Materials and Experimental Method

❒ *Raw material investigations and methods used*

Taking into account the information offered by the phase diagram presented in Fig.4, the alloy for this study was prepared using the following stoichiometry: 50 wt. % Fe and 50 wt. % Ti. The starting materials to produce the intermetallic compound TiFe were elemental Ti (-100 mesh, 99.4% purity) and Fe (<10 micron, 99.9+%), from AlfaAesar.

Before starting the dosing and blending operations, the powders were first characterized. The particle size and granulometric distribution of the elemental powders was determined by laser diffraction. Crystal structure and constituent phases in the materials were determined by XRD. The morphology of the materials was studied by SEM analysis.

Characteristics of the initial powders

X-ray diffraction (XRD) analysis was performed to identify the crystalline phases present in the samples and to determine the corresponding lattice parameters. Fig. 5 presents the diffractograms obtained, recorded using a X'PERT PRO MPD diffractometer, in a Bragg-Brentano geometry. Phase identification was performed by comparing the positions and relative intensities of the experimental diffraction peaks with reference data from ICDD PDF4+ database.

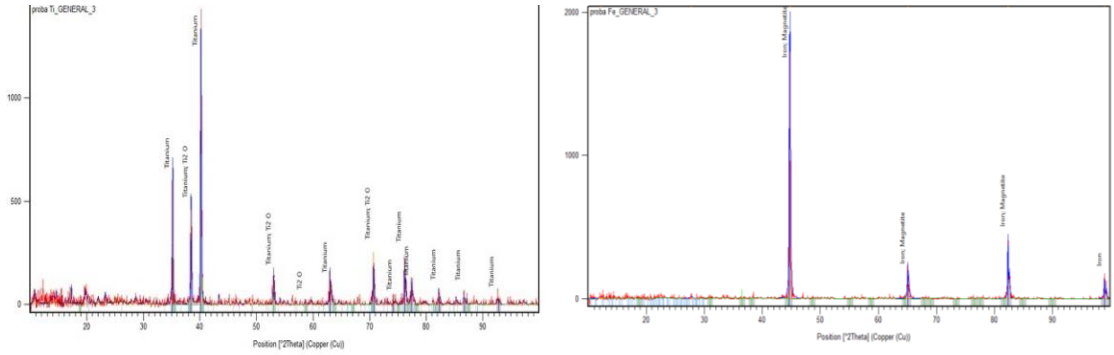

Fig 5. X-ray diffraction (XRD) patterns of the initial powders

Ti (left) Fe (right)

For titanium powder, the XRD calitative analysis indicated a HCP crystal system (□-Ti). The main identified compounds were Ti and Ti2O; semi quantitative analysis revealed the following composition: 87% Ti, 13% Ti2O. Main peaks were identified as Ti, corresponding to the characteristic diffraction peaks located at the following 2θ values: 40.171 deg, 38.411 deg, 35.092 deg, 62.955 deg.

For iron powder the main compounds identified were Fe (BCC) and magnetite; semi quantitative analysis revealed 93% Fe, 7% magnetite. Main peaks were identified as Fe, corresponding to the characteristic diffraction peaks located at the following 2θ values: 44.713 deg, 82.419 deg, 65.084 deg, 116.537 deg.

Fig. 6 presents the images obtained by SEM analysis, using secondary electrons detector, 30 kV acceleration tension for Ti and 10 kV Fe.

For Fe, images were taken at different magnifications: 1000× (overview) and 4000× (detailed view), as shown in Fig. 6a. Spherically shaped particles can be observed, well-defined, with smooth surfaces, free of asperities, and rounded contours. Smaller particles are attached to the larger ones, forming agglomerates.

For Ti, images were obtained at magnifications of 500× and 1000× (detailed view), as shown in Fig. 6b. Particles of varying sizes can be observed, with irregular and angular geometries. Some smaller particles are attached to the larger ones (these are referred to as “satellite” particles).

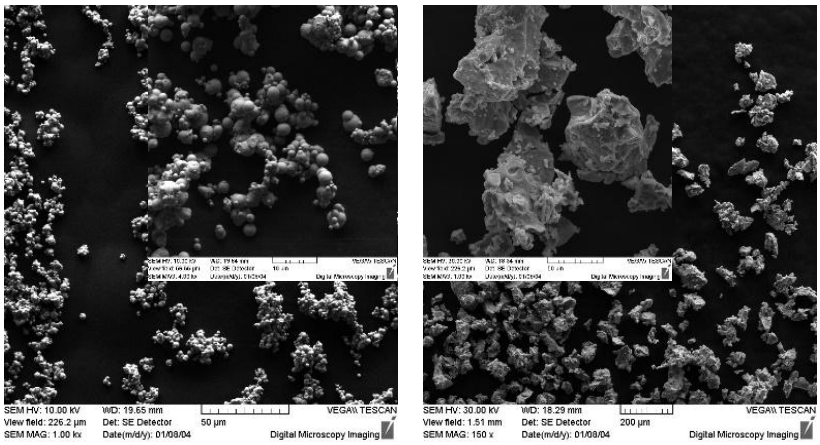

Fig 6. SEM micrographs of the initial powders

a. – Fe 1000x magnification (detail at 4000x)
b. – Ti 150x magnification (detail at 1000x)

Fig. 7 presents the granulometric distribution of Ti and Fe powders used in the experiments. The particle size distribution was determined by laser diffraction, using a stirring time of 5 seconds without ultrasonication, with water as the dispersion medium.

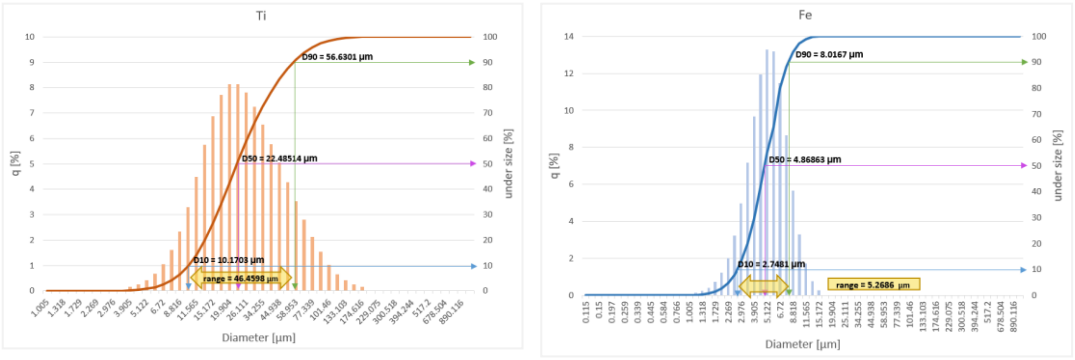

Fig. 7 Granulometric distribution of the initial powders

For the titanium powder, the obtained histogram exhibits a single well-defined peak, indicating a monomodal distribution, with particle diameters ranging from 3.9 µm to 175 µm. The highest frequency (q%) was recorded for diameters between 17 and 30 µm, corresponding to the fine particle range. The cumulative curve shows a progressive and continuous increase with a moderate slope. The particle size distribution analysis reveals a moderately wide dispersion of particles,

with the following characteristic values: D10 = 10.1703 µm, D50 = 22.48514 µm, and D90 = 56.6301 µm. The mean diameter is 29.06461 µm, slightly higher than the median diameter D50. The size range (D90 – D10) is 46.4598 µm, representing the main size interval in which most particles are found.

For the iron powder, the obtained histogram is narrow and shows a single well-defined peak, indicating a monomodal distribution, with particle diameters ranging from 1.5 µm to 15 µm, which denotes that the powder is very fine. The highest frequency (q%) was recorded for diameters between 5 and 6 µm, corresponding to the very fine particle range. The cumulative curve exhibits a progressive and continuous increase with a steep slope, indicating a faster transition from very fine to slightly larger particles. The particle size distribution analysis reveals a high degree of particle homogeneity, with the following characteristic values: D10 = 2.7481 µm, D50 = 4.86863 µm, and D90 = 8.0167 µm. The mean diameter is 5.18065 µm, very close to D50, indicating an almost symmetric distribution without significant skew toward finer or coarser particles. The size range (D90 – D10) has a value of 5.2686 µm.

❒ *Sintering method and parameters*

As synthesis method, powder metallurgy was chosen based on the advantages of this method: alternative method for manufacturing cheaper Ti alloys [28], is near-net-shape method which drastically reduces machining costs and increases material yield, allows new alloys design, as it prevents the segregation of alloy elements that can occur during ingot metallurgy solidification [29].

According to the used raw powders, titanium alloys synthesized via powder metallurgy (PM) can be classified into: pre-alloyed PM Ti alloys, and blended elemental PM Ti alloys [30]. For this paper, a blend of elemental powders was used in preparing TiFe alloy, adopting the flow presented in Fig. 8.

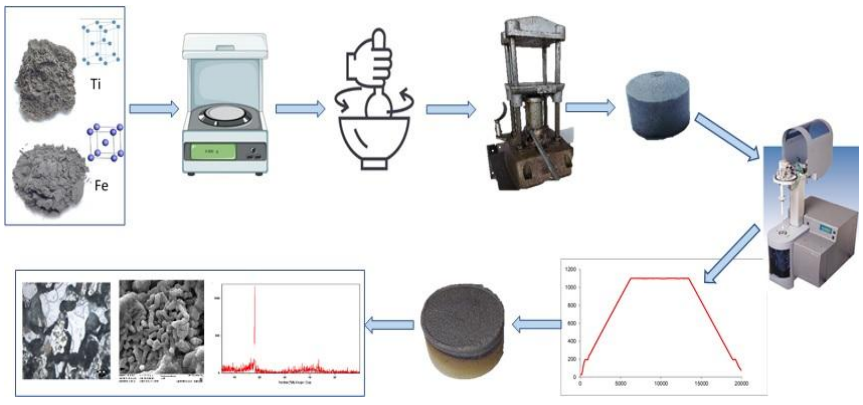

Fig 8. Flow used in obtaining TiFe sintered compacts

After dosage and manual blending of the elemental Ti and Fe powders (using mortar and pestle), pressing was performed, using an uniaxial manual press, at ~5 MPa, obtaining a green TiFe compact, as presented in Fig. 9a.

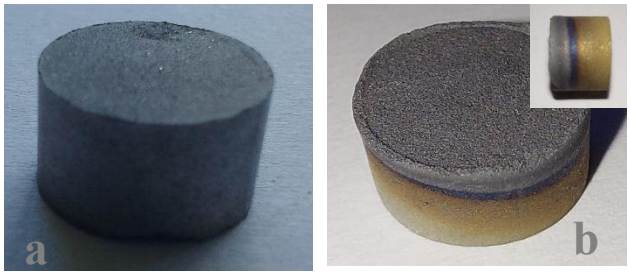

Fig 9. TiFe compact
a. – green b. - sintered

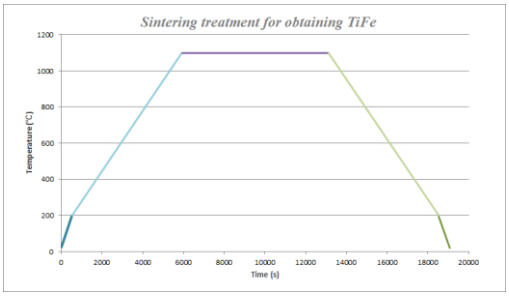

Fig 10. Sintering diagram

Next, sintering was performed, in a SETARAM SETSYS EVOLUTION 24 thermal analyzer, at 1085°C, in Ar inert atmosphere (Ar 4.6 – 99.996 % purity), at atmospheric pressure. The sample was placed in a crucible, and the following sintering treatment was applied (illustrated in Fig. 10):

- 25°C - 200°C, 20°C/min heating rate;
- 200°C - 1100°C, 10°C/min heating rate;
- 1100°C isothermal hold, for 120 min
- 1100 °C - 200°C, 10°C/min cooling rate;
- 200°C - 25°C -, 20°C/min cooling rate.

For controlling and recording the functioning parameters, SETSOFT 2000 software was used and the experimental data were exported and processed.

After the sintering treatment, sintered TiFe compact was obtained (Fig. 9b.). Visual and dimensional examination were performed and then, the sample was longitudinally cut, polished and half of the sample was embedded in conductive resin (for Vickers hardness determinations). Then, the sample was analyzed, using different examination techniques.

❒ *Sintered product characterization techniques*

X-ray diffraction (XRD) measurements were performed using a Rigaku SmartLab diffractometer, equipped with an X-ray generator featuring a Cu Kα anode, operated at an accelerating voltage of 40 kV and a current of 5 mA. The Bragg–Brentano (θ–2θ) geometry was used. Data acquisition was carried out over an angular range of 2θ = 5–90°, with a scan step of 0.01° and a scan rate of 5° min^{-1}. Phase identification was performed using SmartLab Studio II software and the International Centre for Diffraction Data (ICDD, PDF-5+) database.

Surfaces morphology and microstructures was analyzed by light microscopy, using an optical microscope, OLYMPUS GX71 type, and AnalySIS software for processing and archiving the obtained images.

The morphology of the material was studied by SEM analysis, using a TESCAN VEGA II LMU scanning electron microscope, which permitted to obtain secondary electrons (SE) and backscattered electrons (BSE) images.

Vickers hardness testing was performed at room temperature, using a OPL micro hardness tester, in automatic cycle, at 100 gf micro charge.

3. Results and Discussions

❒ *Dimensional parameters and porosity evaluation*

After sintering, the obtained sample was measured:

- height and diameter, using a micrometer, ± 0.001 mm precision;
- mass, using an analytical balance, ± 0.00001 g precision.

The obtained values were analyzed, compared to the ones obtained for the green compact, the results being presented in Table 1. Based on these measurements, the porosity of the compact and degree of densification was estimated.

Table 1.

Sample dimensions and porosity evaluation

Parameter	Green TiFe compact	Sintered TiFe compact	Observations
Φ [mm]	9.429	9.285	Slight radial contraction
h [mm]	5.407	5.078	Noticeable axial contraction
m [g]	1.45883	1.47795	Very slight increase
ρ_{geom} [g/cm^3]	3.866	4.301	Increase due to pore elimination
V_{tot}[cm^3]	0.377	0.344	Decrease of approximately 9% (densification)
ρ_{theor} [g/cm^3]	5.730	5.730	
estimated porosity [%]	~ 32.5	~ 25 %	Reduction through sintering
V_{solid} [cm³]	0.255	0.258	Slight increase (attributed to the higher mass after sintering)
V_{pores} [mm³]	0.123	0.086	Reduction of approximately 30%
Degree of densification -η [%]	-	30	Efficient sintering process

Used formulas:

$\rho_{geom} = 4 \cdot m / \pi \cdot D^2 \cdot h$

$V_{tot} = \pi D^2 \cdot h / 4$ *(total volume of the sample)*

$V_{solid} = m / \rho_{theor}$ *(volume of the solid sample, without pores)*

$V_{pores} = V_{tot} - V_{solid}$ *(volume of pores remained after sintering)*

$Porosity = 1 - \rho_{geom} / \rho_{theor}$

$\eta = [(Vpores\ green - Vpores\ sintered) / Vpores\ green\ ] \times 100$

As observed in Tab. 1, the mass measurements of the samples indicated a slight increase in mass, which can be attributed to the impurities present in the gas. At high temperatures, these trace impurities can react with the material (especially with Ti, which is very reactive. Another possible explanation for the slight increase in mass may be attributed to the possibility that the working gas (Ar) penetrates into the material through pores open to the free surface, followed by its diffusion into the bulk via interconnected pores.

It is also noted that the sintering process led to the densification of the compact and a reduction in porosity, achieving approximately 75% of the theoretical density—a value frequently reported in the literature. Higher densities (>75%) can be obtained at compaction pressures of approximately 500 MPa.

The reduction in pore volume after thermal treatment treatment was further evidenced by porosity estimation and calculations for the remaining pore volume after sintering, the results being presented in Tab. 1. Based on these values, the degree of densification was estimated to be approximately 30%, indicating an efficient process that effectively reduced both pores and void spaces between particles.

❒ *XRD*

For observing if the intermetallic TiFe compound was obtained, phase analysis was performed by XRD (on the longitudinal cross section of the sintered compact) using WPPF. Fig. 11 presents the obtained pattern and also the Rietveld refinement.

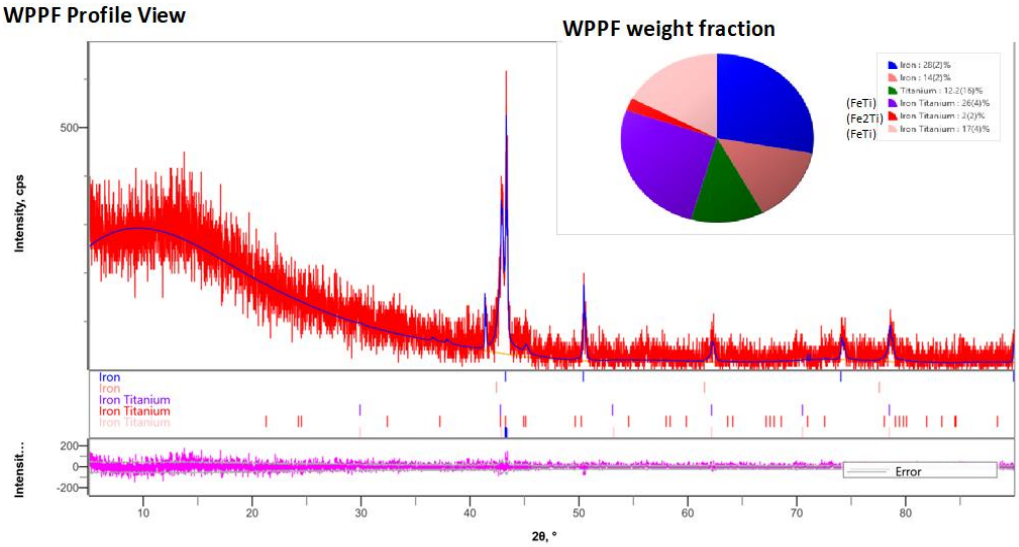

Fig 11. XRD pattern and Rietveld refinement on the sintered sample

The crystalline phases were identified based on the positions of the diffraction maxim (2θ), the interplanar spacings calculated according to Bragg's law (d), and the characteristic reflections indexed using Miller indices (hkl). Following analysis of the obtained diffraction pattern and phase identification using the ICDD, PDF-5+ database, the main peaks and characteristic reflections were attributed to the following phases: Fe, Ti, FeTi, and Fe_2Ti. The refinement yielded $\chi^2 = 1.07$, indicating good agreement between the calculated and experimental profiles.

For the compound of interest, TiFe, the identified phase exhibits a cubic B2 structure (CsCl-type), with a lattice parameter a = 2.98 Å, consistent with values reported in the literature. The formation of TiFe intermetallic compound was confirmed by its characteristic reflections: (110) at $2\theta \approx 42.8°$, (200) at $2\theta \approx 62.1°$, and (211) at $2\theta \approx 78.4°$. Quantitative analysis indicated a fraction of 43% equiatomic TiFe (1:1), confirming the partial formation of the TiFe intermetallic phase.

The presence of residual Fe and Ti, together with slight deviations in lattice parameters, suggests possible structural distortions caused by the formation of Fe–Ti solid solutions or diffusion zones, in which elemental diffusion had initiated but the sintering conditions were insufficient to ensure complete interaction.

The presence of a minor $TiFe_2$ phase (2%), with a Laves-type structure, may be attributed to a local excess of Fe and the continuation of the FeTi + Fe reaction in certain regions beyond the ideal 1:1 stoichiometry.

❒ *Light microscopy*

The microstructure of TiFe alloys depends on the composition, sintering temperature and the post processing method (thermal treatment). Fig. 12a presents a micrograph obtained from the longitudinal section of the sample, without a chemical attack.

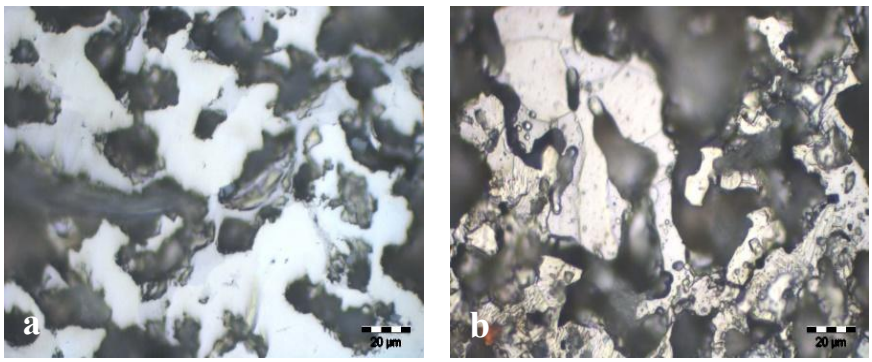

Fig 12. Optical microscopy on the sintered TiFe compact

a. – before chemical attack b. – after chemical attack

Fig. 12b presents the images obtained by optical microscopy, after a chemical attack (fluoro-nitric type, using 2 ml HF, 4 ml HNO_3, 100 ml H_2O), in order to better reveal the microstructure and homogeneity. It can be observed that the chemical attack produced distinct reactions, depending on the constituents of the mixture. The light contrast of the image indicates a clear differentiation between Ti-rich and Fe-rich regions, as a consequence of limited diffusion. The residual porosity is pronounced and unevenly distributed, indicating low densification. This reflects both the low reactivity between Fe and Ti and insufficient diffusion for pore elimination. The resulting microstructure is typical of incomplete sintering in metallic systems with high melting points and significant differences in diffusivity.

❒ ***SEM***

The sintered compact was analyzed in longitudinal cross section, at different magnifications and in different zones, using SE and BSE (backscattered electrons) (Fig. 13). The microstructure indicates a significant proportion of pores, which may originate prom the mixing and compaction process, as well as from incomplete sintering. The brightness contrast suggests a multiphase distribution.

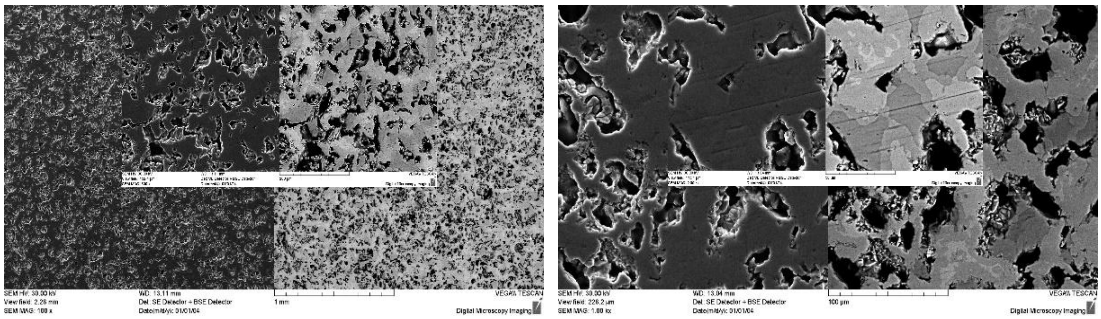

Fig 13. SEM images, obtained with SE and BSE
100x with details at 500x (left) and 1000x with details 2000x (right)

❒ ***EDX***

The longitudinal cross section of the sintered compact was also analyzed by EDX Energy Dispersive X-ray Spectroscopy). Examinations were performed in SE and BSE (backscattered electron imaging) modes, at 1000x magnification (Fig. 14).

As in the case if light microscopy, the presence of pores is noted.

The sample analyzed presents several shades of gray. These differences in contrast suggest variations in the chemical composition throughout the alloy. For this reason, EDX analysis was performed, in point scan mode, choosing 3 points from regions with different light intensities.

EDX analysis provided the energy spectrum of X-rays characteristic to the chemical elements in the different points. The obtained spectra highlighted the presence of iron and titanium.

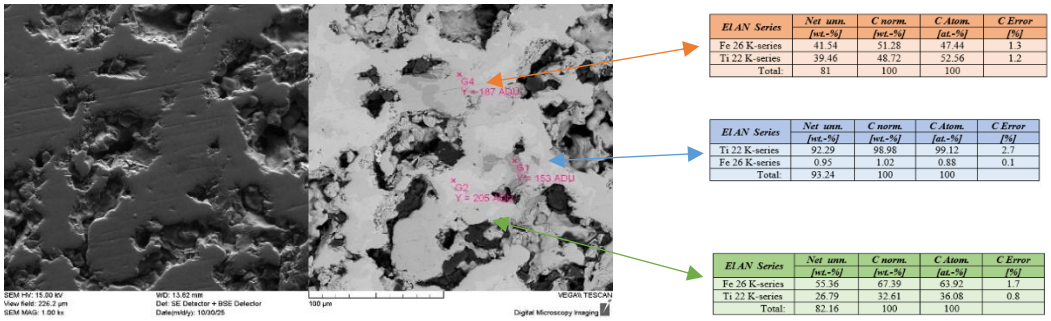

EDAX Series	Net unn. [wt.-%]	C norm. [wt.-%]	C Atom. [at.-%]	C Error [%]
Fe 26 K-series	41.54	51.28	47.44	1.3
Ti 22 K-series	39.46	48.72	52.56	1.2
Total:	81	100	100	

EDAX Series	Net unn. [wt.-%]	C norm. [wt.-%]	C Atom. [at.-%]	C Error [%]
Ti 22 K-series	92.29	98.98	99.12	2.7
Fe 26 K-series	0.95	1.02	0.88	0.1
Total:	93.24	100	100	

EDAX Series	Net unn. [wt.-%]	C norm. [wt.-%]	C Atom. [at.-%]	C Error [%]
Fe 26 K-series	55.36	67.39	63.92	1.7
Ti 22 K-series	26.79	32.61	36.08	0.8
Total:	82.16	100	100	

Fig. 14 EDX images and quantitative analysis

Quantitative analysis showed that the three studied points corresponds to:

- a zone highly enriched in Ti, in G1, with 98.98 % Ti and 1.02 % Fe;
- a zone with high Fe content, in G2, with 67.39 % Fe and 32.61 % Ti;
- a zone attributed to TiFe compound, in G4, where the two elements are in almost equal percent: 51.28 % Fe and 48.72 % Ti.

EDX mapping (Fig. 15) indicated a relatively uniform distribution of the alloying elements. However, it can be observed that certain areas exhibit higher concentrations of Fe, while others are richer in Ti.

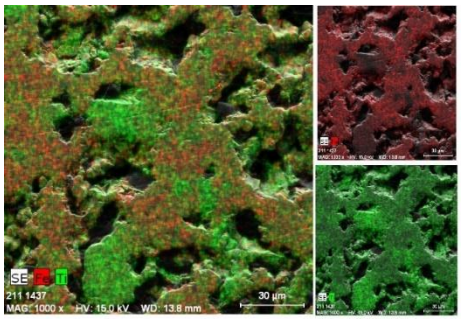

Fig. 15 EDX mapping

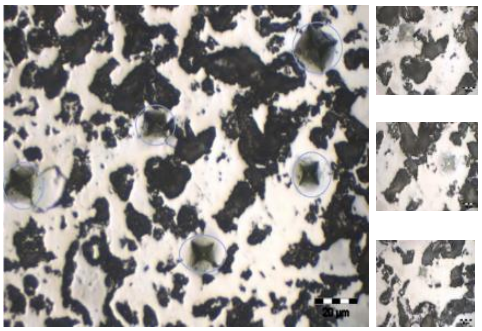

Fig 16. Optical microscopy and hardness imprints

❒ *Hardness*

The micro hardness of intermetallic phases is greater than the ones for pure metals, so the Vickers hardness can be useful to locate the possible formation of the intermetallic compound. In order to evaluate the hardness of the sintered sample, in different areas, Vickers hardness test was performed in 5 different points of the sample (transversal cut and embedded in Cu resin). Fig. 16 presents the hardness imprints, with details for some of the individual marks.

The micro hardness determined values varied between ~450 – 200 HV. According to the values reported in literature for TiFe 50 wt.%, the Vickers hardness is ~400. The measurements showed the difference between the harnesses on the surface of the analyzed sample, indicating a non-uniformity.

5. Conclusions

In this preliminary study, the possibility of synthesizing TiFe intermetallic using the powder metallurgy method was explored and evaluated, considering the potential of this material for hydrogen storage application. Structural and morphological analyses (XRD, SEM, optical microscopy, and microhardness testing) confirmed the partial formation of the TiFe phase in specific regions of the samples, indicating that the employed route can be suitable for obtaining this compound. The results obtained in this study demonstrate that the powder metallurgy method, through sintering, is suitable for the synthesis of the TiFe intermetallic compound.

However, the experimental conditions employed were insufficient to achieve a single-phase TiFe intermetallic compound with a homogeneous elemental distribution. Possible causes include:

- inhomogeneity of the initial powder mixture → since a ball mill was not available, mixing was performed manually, which resulted in a low degree of homogenization, favoring particle segregation and local compositional variations;
- differences in particle size between the constituent powders → may have contributed to uneven diffusion and reaction kinetics;
- insufficient compaction → manual uniaxial pressing possibly did not provide the pressure level or control required for adequate densification of the powder mixture;
- insufficient applied pressure → may generate voids, leading to increased porosity in the green compacts;
- relatively short sintering time → limited the extent of interdiffusion and phase formation;
- potential need for post-synthesis thermal treatments → to promote further diffusion and phase homogenization.

Collectively, these factors contributed to insufficient elemental diffusion and incomplete formation of the TiFe intermetallic phase. Future research will therefore focus on fine-tuning these parameters, as well as investigating the hydrogen absorption–desorption behavior of the optimized samples, in order to establish clear correlations between microstructure, mechanical properties, and hydrogen storage performance.

Overall, the findings provide a valuable basis for the continued development of efficient intermetallic compounds for sustainable energy and hydrogen storage systems.

REFERENCES

[1] *M. Ball and M. Weeda*, The hydrogen economy – Vision or reality?, International Journal of Hydrogen Energy, vol. **40**, no. 25, pp. 7903-7919, 2015.

[2] BLUE PLANET, Hydrogen - Blue Planet, [Online]. Available: https://blueplanet.gr/hydrogen. [Accessed 13 05 2025].

[3] *B. Seemita*, Studies on Advanced Materials for Hydrogen Storage, Mumbai: A thesis submitted to the Board of Studies in Chemical Sciences In partial fulfillment of requirements For the Degree of DOCTOR OF PHYLOSOPHY of HOMI BHABHA NATIONAL INSTITUTE, 2013.

[4] *M. G. Shelyapina*, Metal Hydrides for Energy Storage, Handbook of Ecomaterials, pp. 775-810, 2019.

[5] *K. Shashikala*, Hydrogen Storage Materials, Functional Materials, pp. 607-637, 2012.

[6] *M. V. Lototskyy, B. P. Tarasov and V. A. Yartys*, Gas-phase applications of metal hydrides, Journal of Energy Storage, vol. **73**, p. 108165, 2023.

[7] *A. Züttel*, Materials for Hydrogen Storage, Catalysis for Sustainable Energy Production, pp. 107-169, 3 2009.

[8] *Fraunhofer Institute for Manufacturing Technology and Advanced Materials IFAM,* Applications of metal hydrides, [Online]. Available: https://www.ifam.fraunhofer.de/en/Aboutus/Locations/Dresden/HydrogenTechnology/hydrides/applications-of-metal-hydrides.html. [Accessed 20 05 2025].

[9] *J. Andersson and S. Grönkvist*, Large-scale storage of hydrogen, International Journal of Hydrogen Energy, vol. **44**, no. 23, pp. 11901-11919, 5 2019.

[10] *M. M. D. Roy, A. A. Omaña, A. S. S. Wilson, M. S. Hill, S. Aldridge and E. Rivard*, Molecular Main Group Metal Hydrides, Chemical Reviews, vol. **121**, no. 20, pp. 12784-12965, 10 2021.

[11] *S. Ali, N. Abbas, S. A. Khan, I. Malik and M. Mansha*, Chemical-based Hydrogen Storage Systems: Recent Developments, Challenges, and Prospectives, Chemistry – An Asian Journal, vol. **19**, no. 16, 8 2024.

[12] *Z. Chen, Z. Ma, J. Zheng, X. Li, E. Akiba and H.-W. Li*, Perspectives and challenges of hydrogen storage in solid-state hydrides, Chinese Journal of Chemical Engineering, vol. **29**, pp. 1-12, 1 2021.

[13] *E. M. Dematteis, D. M. Dreistadt, G. Capurso, J. Jepsen, F. Cuevas and M. Latroche*, Fundamental hydrogen storage properties of TiFe-alloy with partial substitution of Fe by Ti and Mn, Journal of Alloys and Compounds, vol. **874**, p. 159925, 9 2021.

[14] *K. B. Park, W.-S. Ko, J. O. Fadonougbo, T.-W. Na, H.-T. Im, J.-Y. Park, J.-W. Kang, H.-S. Kang, C.-S. Park and H.-K. Park*, Effect of Fe substitution by Mn and Cr on first

hydrogenation kinetics of air-exposed TiFe-based hydrogen storage alloy, Materials Characterization, vol. **178**.

[15] *Y. Liu, D. Chabane and O. Elkedim*, Intermetallic Compounds Synthesized by Mechanical Alloying for Solid-State Hydrogen Storage: A Review, Energies, vol. **14**, 2021.

[16] *E. Alvares, P. Jerabek, Y. Shang, A. Santhosh, C. Pistidda, T. W. Heo, B. Sundman and M. Dornheim*, Modeling the thermodynamics of the FeTi hydrogenation under para-equilibrium: An ab-initio and experimental study, Calphad, vol. **77**, 2022.

[17] *Royal Society of Chemistry*, Titanium – Element information,properties and uses | Periodic Table, [Online]. Available: https://periodic-table.rsc.org/element/22/titanium. [Accessed 20 05 2025].

[18] *Royal Society of Chemistry*, Iron – Element information,properties and uses | Periodic Table, [Online]. Available: https://periodic-table.rsc.org/element/26/iron. [Accessed 20 06 2025].

[19] *F. Laves and H. J. Wallbaum*, Zur Kristallchemie von Titan- Legierungen, Naturwissenschaften, p. 674–675, 1939.

[20] Z. Z. Fang et al., "Powder metallurgy of titanium – past, present, and future," International Materials Reviews, vol. 63, no. 7, pp. 407–459, Oct. 2018, doi: 10.1080/09506608.2017.1366003.

[21] Y. Liu, L. F. Chen, H. P. Tang, C. T. Liu, B. Liu, and B. Y. Huang, "Design of powder metallurgy titanium alloys and composites," Materials Science and Engineering: A, vol. 418, no. 1–2, pp. 25–35, Feb. 2006, doi: 10.1016/j.msea.2005.10.057.

[22] L. Bolzoni, F. Yang, and M. Paul, "Development and characterisation of low-cost powder metallurgy Ti–Cu–Fe alloys," Journal of Materials Research and Technology, vol. 24, pp. 2678–2687, May 2023, doi: 10.1016/j.jmrt.2023.03.178

[23] S. Raynova, M. A. Imam, F. Yang, and L. Bolzoni, "Hybrid microwave sintering of blended elemental Ti alloys," Journal of Manufacturing Processes, vol. 39, pp. 52–57, Mar. 2019, doi: 10.1016/j.jmapro.2019.02.002.

[24] L. Bolzoni, E. Herraiz, E. M. Ruiz-Navas, and E. Gordo, "Study of the properties of low-cost powder metallurgy titanium alloys by 430 stainless steel addition," Materials & Design, vol. 60, pp. 628–636, Aug. 2014, doi: 10.1016/j.matdes.2014.04.019.

[25] C. Romero, F. Yang, S. Wei, and L. Bolzoni, "Thermomechanical Processing of Cost-Affordable Powder Metallurgy Ti-5Fe Alloys from the Blended Elemental Approach: Microstructure, Tensile Deformation Behavior, and Failure," Metals, vol. 10, no. 11, p. 1405, Oct. 2020, doi: 10.3390/met10111405.

[26] C. Romero, F. Yang, S. Raynova, and L. Bolzoni, "Thermomechanically processed powder metallurgy Ti-5Fe alloy: Effect of microstructure, texture, Fe partitioning and residual porosity on tensile and fatigue behaviour," Materialia, vol. 20, p. 101254, Dec. 2021, doi: 10.1016/j.mtla.2021.101254.

[27] A. *I. Osman, A. Ayati, M. Farrokhi, S. Khadempir, A. R. Rajabzadeh, M. Farghali, P. Krivoshapkin, B. Tanhaei, D. W. Rooney and P.-S. Yap*, Innovations in hydrogen storage materials: Synthesis, applications, and prospects, Journal of Energy Storage, vol. **95**, p. 112376, 8 2024.

[28] *P. K. Manne, N. S. Kumar, T. Buddi, A. A. Lakshmi and R. Subbiah*, Powder Metallurgy Techniques for Titanium Alloys-A Review, in E3S Web of Conferences 184, 2020.

[29] *E. Reverte, S. A. Tsipas and E. Gordo*, Oxidation and Corrosion Behavior of New Low-Cost Ti-7Fe-3Al and Ti-7Fe-5Cr Alloys from Titanium Hydride Powders, Metals, vol. **10**, p. 254, 2020.

[30] *Y. Liu, L. F. Chena, H. P. Tang, C. T. Liu, B. Liua and B. Y. Huang*, Design of powder metallurgy titanium alloys and composites, Materials Science and Engineering: A, vol. **418**, pp. 25-35, 2006.